# Sterically Invariant Carborane-Based Ligands for the Morphological and Electronic Control of Metal-Organic Chalcogenolate Assemblies

Harrison A. Mills<sup>a</sup>, Christopher G. Jones<sup>a,b</sup>, Kierstyn P. Anderson<sup>a</sup>, Austin D. Ready<sup>a</sup>, Peter I. Djurovich<sup>c</sup>, Saeed I. Khan<sup>a</sup>, J. Nathan Hohman\*, Hosea M. Nelson\*, Alexander M. Spokoyny\*,a,e

<sup>a</sup>Department of Chemistry and Biochemistry, University of California, Los Angeles, Los Angeles, California 90095, United States

<sup>b</sup>Division of Chemistry and Chemical Engineering, California Institute of Technology, Pasadena, California 91125, United States

<sup>c</sup>Department of Chemistry, University of Southern California, Los Angeles, California 90089, United States

<sup>d</sup>Institute of Materials Science and the Department of Chemistry, University of Connecticut, Storrs, Connecticut 06269, United States

<sup>e</sup>California NanoSystems Institute (CNSI), University of California, Los Angeles, Los Angeles, California 90095, United States

#### Abstract

Herein, we report the use of sterically invariant carborane-based chalcogenols, containing exopolyhedral B-Se or B-S bonds, as ligands for the formation of photoluminescent copper(I)-based metal-organic chalcogenolate assemblies (MOCHAs). We show that precise tuning of the carborane dipole by changing the carborane isomer from *meta*- to *ortho*- allows for control over the MOCHA morphology and regulation of the resulting photophysical properties. Furthermore, microcrystal electron diffraction (MicroED) has been demonstrated as a powerful tool for metal chalcogenide structure elucidation. Through the use of MicroED, one of the isolated materials is determined to consist of zero-dimensional Cu<sub>4</sub>(Se-C<sub>2</sub>B<sub>10</sub>H<sub>11</sub>)<sub>4</sub> clusters with an unprecedented Cu<sub>4</sub>Se<sub>4</sub> geometry.

#### Introduction

Transition metal chalcogenides represent a large class of hybrid materials that have been extensively studied in both academic and non-academic research areas due to their promise as materials for a variety of applications, including photoluminescence,<sup>1-3</sup> electronic devices<sup>4-6</sup> and electrochemical reactions.<sup>7-9</sup> Practitioners have often employed dimensional reduction of bulk materials as a facile strategy to tune and diversify material properties.<sup>10</sup> This strategy of dimensional reduction may utilize either a top down<sup>11-13</sup> or bottom up<sup>14-19</sup> synthetic approach, resulting in the formation of low-dimensional (zero-, one-, or two-dimensional) materials with a variety of architectures and surface compositions. One established method for the bottom-up dimensional control of metal chalcogenides has made use of the inherent reactivity between organic chalcogenols and metal cation-based precursors. The formed structures, more recently referred to as metal-organic chalcogenolate assemblies (MOCHAs, Figure 1a), have shown great promise in the preparation of low-dimensional metal-chalcogenide materials.<sup>20-34</sup> More

specifically, some MOCHAs have been synthesized using a biphasic approach from aqueous metal cations (e.g. copper(I)<sup>20</sup>, silver(I)<sup>24</sup>) layered with chalcogenols (e.g. alkyl thiols, aryl selenols) dissolved in an organic solvent. At the solvent-solvent interface, the organic chalcogenols react with the metal cations forming intermediary metal complexes which then nucleate and propagate the growth of small crystallites. Recently, this approach to MOCHA growth has also been extended to methods utilizing metal surfaces and gaseous benzene selenol or diphenyl diselenide reagents, where nucleation and growth of the material occurs at the solid-vapor interface. <sup>26,32</sup> In all cases, while the metal of choice serves as a general framework for MOCHA properties, the overall morphological, physical, and electronic properties are largely dictated by the chalcogenolate-based ligand chosen to template the material formation. It has been further hypothesized, and shown with adamantane and diamantane thiol reagents, that the steric environment of the organic chalcogenols plays an important role in the crystallite propagation, and is a determining factor of the overall material morphology.<sup>20</sup> Furthermore, the intermolecular forces between adjacent chalcogenolate ligands are also expected to regulate the growth of the crystallites. Critically, with the current ligand scaffolds studied with MOCHAs, it is often impossible to isolate the effect of ligand electronics on MOCHA properties without also altering their steric profile in some way, thereby inadvertently changing the steric interactions between the chalcogenolate ligands while also varying the electrostatic interaction between ligands.

# a. previously studied metal-organic chalcogenolate assemblies (MOCHAs)

Bulk Metal, Metal Chalcogenide, Super Atom Surface

[36-39,42-44,46]

[35]

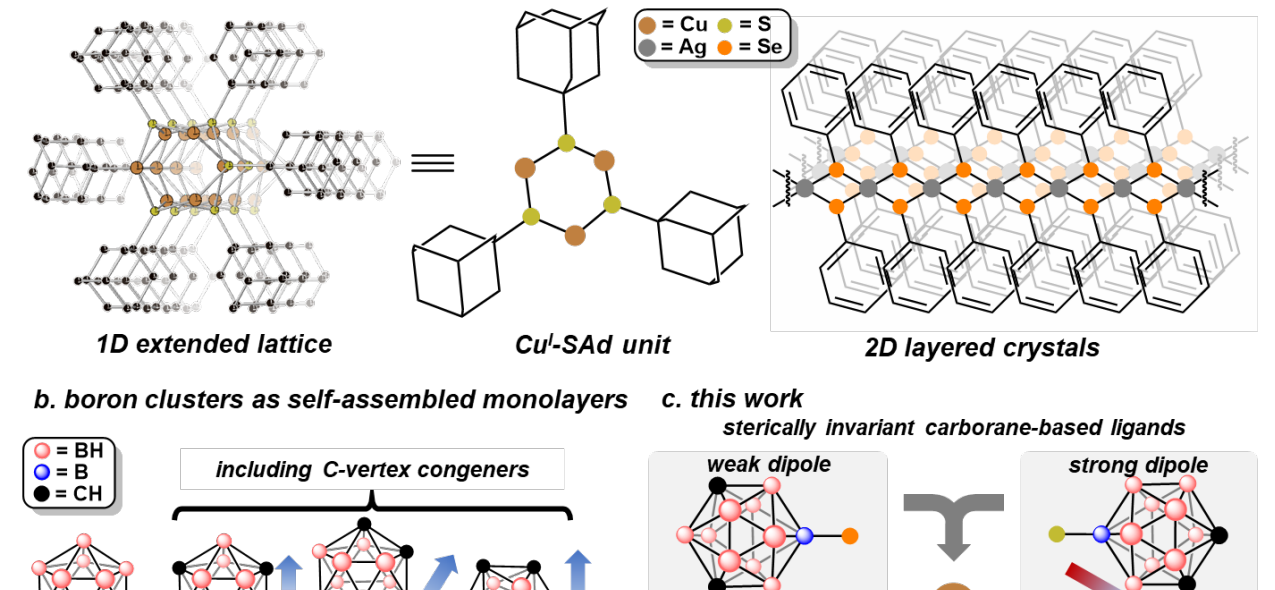


**Figure 1: a.** Selected examples of metal-organic chalcogenolate assemblies (MOCHAs) composed of either copper(I) diamondoid thiolates or silver(I) benzene selenolate. **b.** History of functionalized boron clusters (dodecaborates, carboranes) as self-assembled monolayers on bulk metal, metal chalcogenide, or super atom surfaces. The approximate dipoles of carborane-based ligands have been depicted to the right of the respective ligand. **c.** This work, utilizing sterically invariant carborane-based chalcogenolates to modulate morphology and photophysical properties of carborane-containing MOCHAs.

[48]

One unique class of chalcogen-containing ligands that have not yet been widely explored in the context of MOCHAs are functionalized boron clusters. This is surprising, considering that boron cluster ligands (thiolates, carboxylic acids) have been extensively studied on bulk surfaces for the past two decades, 35-52 and more recently with metal chalcogenide nanoparticles 33-54 as well as metallic super atoms. The attractiveness of boron clusters in these applications is due in large part to their propensity to form "defect-free" monolayers as a function of both the steric bulk provided by the boron cluster and, in the case of neutral boron clusters (i.e. carboranes), their inherent molecular dipole that enables long-range order (Figure 1b). Carboranes, with the

molecular formula of C<sub>2</sub>B<sub>10</sub>H<sub>12</sub>, exist as three distinct isomers (*ortho-*, *meta-*, *para-*) distinguished by the relative orientation of the two carbon vertices. Importantly, the electronic nonuniformity of *ortho-* and *meta-*carboranes, resulting from the asymmetry introduced by the carbon vertices, has allowed for the precise modulation of metal surface<sup>35-57</sup> and metal center properties,<sup>59-65</sup> as determined by the relative positioning of ligating substituents on the sterically invariant boron clusters (Figure 1b). This electronic nonuniformity is further exemplified by the regioselective chemistry of carboranes that has permitted selective introduction of functional groups to the carbon-based vertices and various boron-based vertices of carboranes.<sup>66-68</sup>

Despite the potential for carborane-based ligands to tune MOCHA properties, only two recent studies have reported the use of 9-meta-carboranyl thiolates to generate MOCHA-like structures with cadmium(I)<sup>20</sup> and copper(I).<sup>22</sup> In the case of the cadmium(I)-based MOCHA, the prepared materials were preliminarily visualized by scanning electron microscopy with no additional characterization provided. Conversely, structural characterization of the copper(I)based MOCHA was reported though the study focused solely on the mechanical properties of the resulting materials. To further develop the understanding of structure-function relationships in the context of MOCHAs, and more specifically, the impact a molecular dipole might have on MOCHA morphology and electronic properties, we report our investigation on the formation of copper(I)based MOCHA materials with sulfur and selenium-containing electron-rich carborane chalcogenolates (Figure 1c). Specifically, we show how sterically invariant carborane-based chalcogenolate ligands can control the morphology and electronic properties of copper(I)-based MOCHAs through differences in the carborane dipole between the ortho- and meta- isomers. The morphology, composition, and stability of all reported materials have been determined using scanning electron microscopy (SEM), transmission electron microscopy (TEM), powder X-ray

diffraction (PXRD), Fourier transform infrared spectroscopy (FTIR), thermogravimetric analysis (TGA), and X-ray photoelectron spectroscopy (XPS). Furthermore, critical structural characterization was obtained by applying emerging microcrystal electron diffraction (MicroED) techniques to determine the unique bonding arrangement between copper(I) and 9-meta-carboranyl selenolate for the key MOCHA structure synthesized. All prepared materials exhibit photoluminescence that further exemplify control of MOCHA properties by tuning key photophysical properties, such as quantum yield and emission lifetimes, as a function of both the carborane dipole as well as the chalcogenolate (Se, S) used.

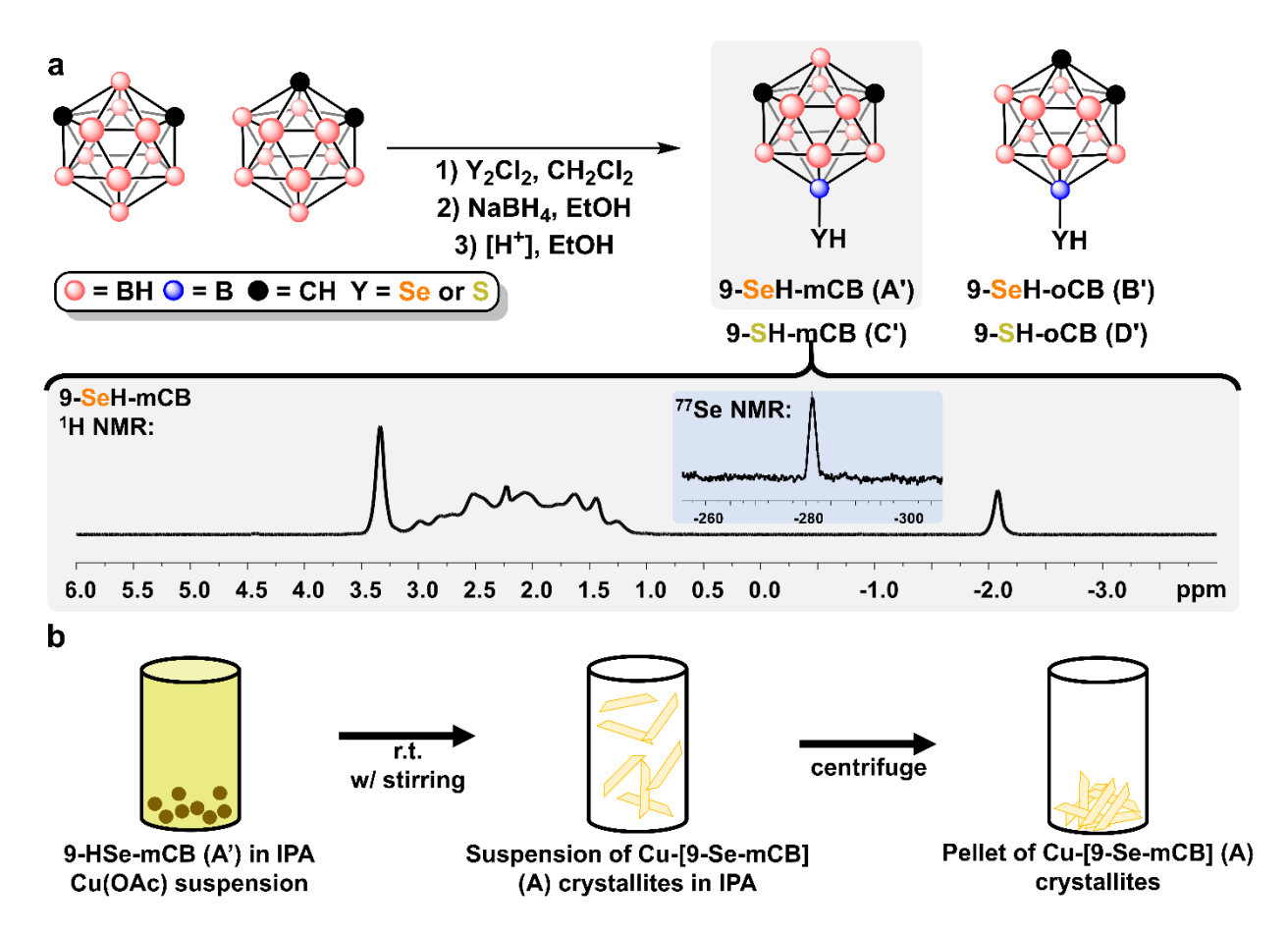


**Figure 2: a.** Synthesis of B(9) substituted *meta*- and *ortho*-carborane selenols and thiols following literature procedures. Representative characterization ( ${}^{1}H$ ,  ${}^{77}Se$  NMR) of 9-SeH-mCB in THF- $d_6$ . **b.** General synthesis of carborane chalcogenolate-containing MOCHAs **A-D**.

# **Results and Discussion**

In order to understand whether one can form MOCHAs with sterically encumbering carborane ligands, we first opted to study the reaction between a copper(I) precursor and 9-metacarboranyl selenol (SeH-mCB, A'). Copper(I) was chosen due to the previously reported reactivity between copper(I) precursors and sterically encumbered adamantane thiol<sup>20</sup> or meta-carboranyl thiol<sup>22</sup> ligands. Conversely, SeH-mCB was selected as our first ligand of study due to the known stability of exopolyhedral B-Se bonds, <sup>69-70</sup> the established body of work utilizing *meta*-carborane ligands in self-assembled materials, 35-57 and lastly, the anticipated reactivity between the selenolate and copper(I). SeH-mCB was synthesized according to literature procedures<sup>69-70</sup> (Figure 2a, SI sec. 3 for full experimental details) and isolated as an air-stable solid that showed little to no oxidation after several months when stored at 5 °C in laboratory air, in contrast to oxidatively unstable carbon-based selenols. To begin our studies regarding the self-assembly behavior of carborane chalcogenols in the presence of copper(I) salts, SeH-mCB and copper(I) acetate were mixed together as powders in a 4 mL dram vial equipped with stir bar in a nitrogen-filled glovebox. Subsequently, anhydrous iso-propanol was added via syringe and the reaction mixture was immediately stirred at 700 rpm in the dark (Figure 2b). This approach takes advantage of gradual etching of the copper(I) acetate particles by the dissolved selenol, decreasing the reaction rate that has previously resulted in non-crystalline MOCHA phases when using benzene selenol.<sup>24</sup> Within minutes, an off-white precipitate began to form, ultimately resulting in a milky suspension after stirring overnight. To separate the formed precipitate, the suspension was centrifuged and the resulting pellet was collected and dried *in vacuo* to remove all volatiles, affording Cu-[Se-mCB] (A) in 76% yield as an analytically pure powder.

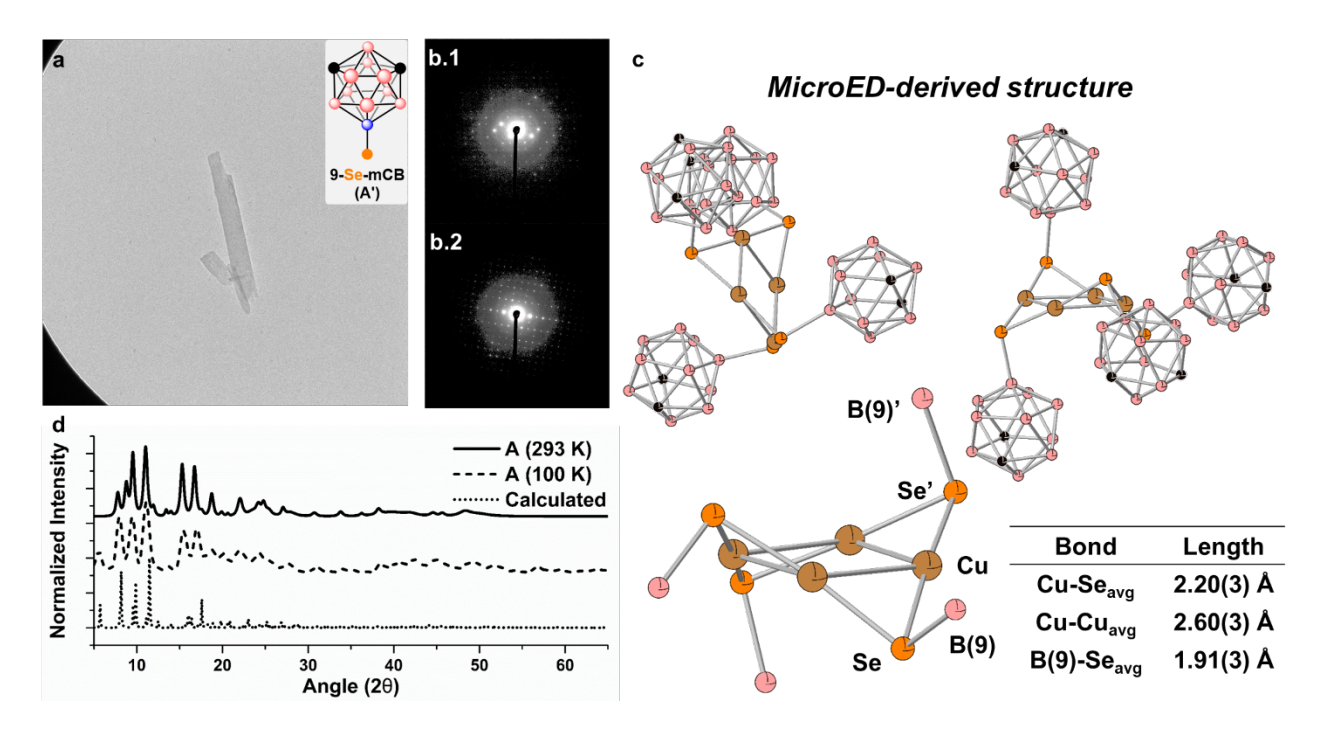


**Figure 3: a.** Representative bright field TEM image of **A** crystallite used for MicroED experiments. **b.** Representative frames of MicroED performed of **A** used for refinement. **c.** MicroED-derived structure of **A** revealing a tetrameric Cu-Se core sterically protected by *meta*-carboranyl ligands. Table provides average bond lengths for relevant bonds. The packing of two clusters is also depicted, showing the proximity of the *meta*-carborane cluster to an adjacent selenolate **d.** PXRD pattern of bulk **A** at 293 K and 100 K, as well as the simulated PXRD pattern from the MicroED-derived structure. Hydrogens have been omitted for clarity.

When visualizing powders of **A** through electron microscopy (TEM, SEM), the morphology of the crystallites was revealed to be square rods, approximately 5-10  $\mu$ m in length and 1-2  $\mu$ m in width (Figures 3a and 4a, SI sec. 5a), somewhat reminiscent of previously imaged MOCHAs composed of Cd-[S-mCB].<sup>20</sup> The crystallinity of the **A** microcrystals present on the TEM sample grid was confirmed using selected area electron diffraction (SAED) (Figure 3b). After observing single crystal diffraction using SAED, MicroED methods were applied for crystallographic analysis of **A**. Despite being highly crystalline, the crystal morphology of **A** microcrystals (square rods) and low symmetry presented a particular challenge as sampling the entirety of reciprocal space was limited due to the range of the TEM sample holder tilt axis. However, by combining data sets from five different microcrystals, sufficient unique reflections

were obtained for an ab initio solution resulting in successful structural determination (see SI for full experimental details). In contrast to previously reported materials with copper(I) diamondoid thiolates<sup>20</sup> or silver(I) benzene selenolates<sup>24</sup> containing an extended metal-chalcogenolate network ([M-SR/SeR]<sub>∞</sub>), A crystallites are comprised entirely of isolated tetrameric copper carborane selenolate clusters with a Cu<sub>4</sub>Se<sub>4</sub> core surrounded by four *meta*-carboranyl ligands, indicating a zero-dimensional morphology (Figure 3c). Surprisingly, the experimentally determined structure of A is highly reminiscent to that observed in the previously reported copper(I) meta-carboranyl thiolate material which adopted a Cu<sub>4</sub>S<sub>4</sub> structure.<sup>22</sup> While the C-H vertices of the *meta*-carboranyl ligands cannot be immediately distinguished, the positioning of the exopolyhedral B(9)-Se bond and anticipated dipole-Se interactions between adjacent meta-carboranyl selenolates have been used to determine the exact positioning of the carbon-based vertices (Figure 3c). Notably, the Cu<sub>4</sub>Se<sub>4</sub> core in **A** is the first structurally characterized copper(I) selenide tetramer with a planar Cu<sub>4</sub> geometry, the formation of which can likely be correlated to the steric bulk of the carboranyl ligands (SI sec. 9). To confirm the validity of the crystal structure obtained via MicroED, experimental PXRD data of A was compared to the simulated PXRD generated from the single crystal MicroED structure (Figure 3d). We observed good agreement between the experimental and simulated PXRD patterns despite some minor deviations that could likely be attributed to thermal contraction of the crystallites while performing MicroED. To confirm that this is the case, PXRD experiments were performed while cooling the crystallites to 100 K with liquid nitrogen (Figure 3d, SI sec. 5b). Importantly, the cryogenic PXRD pattern more closely matches the simulated PXRD pattern, suggesting that the single crystal structure obtained via MicroED is characteristic of the bulk material.

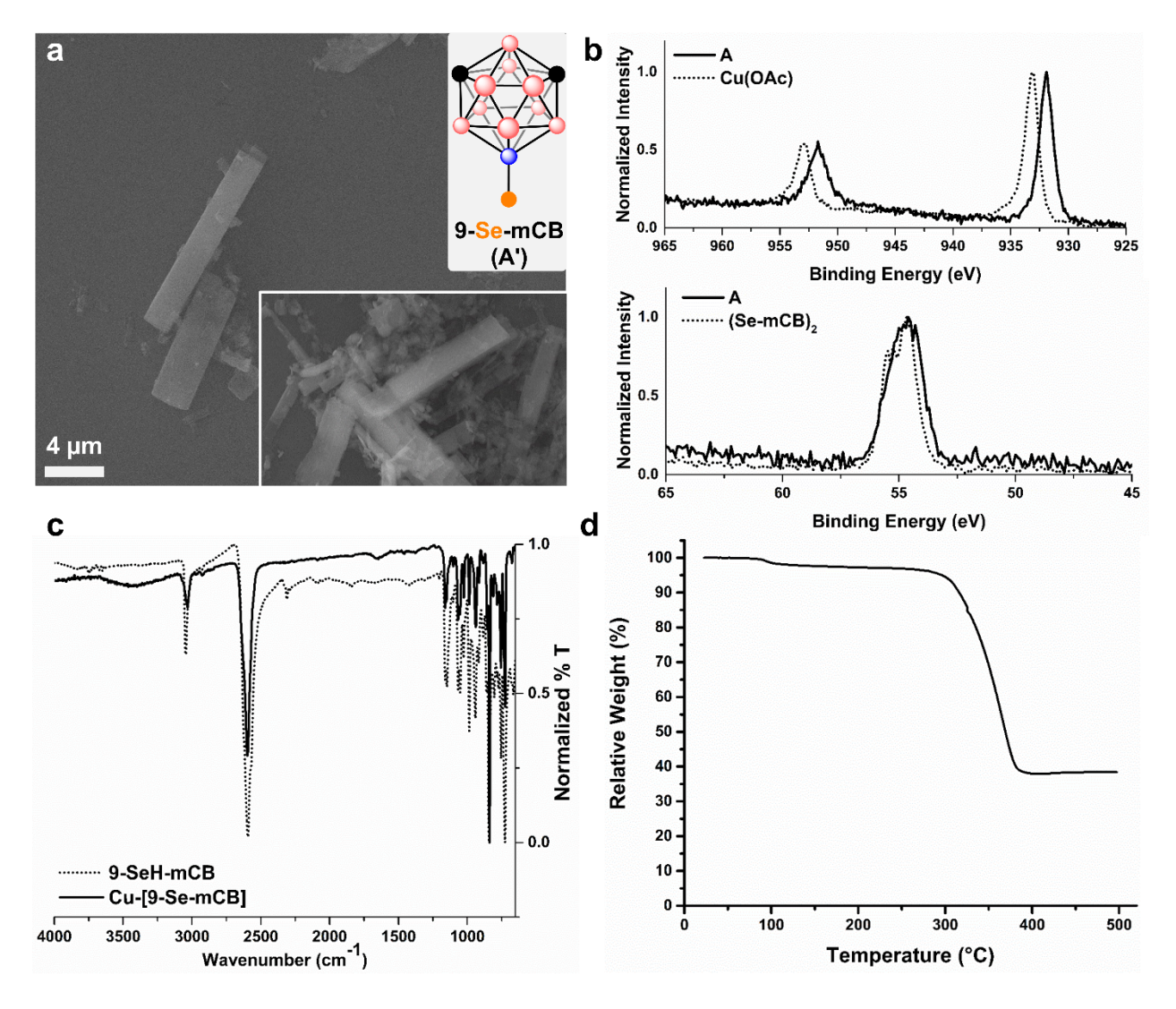


**Figure 4: a.** SEM images of **A.** Inset shows a more general overview of crystallite morphology. Scale bar is applied to both SEM images. **b.** XPS measurements of **A**, Cu(OAc), and (Se-mCB)<sub>2</sub>. **c.** FTIR of 9-SeH-mCB (dotted trace) and **A** (solid trace). **d.** TGA of **A**.

Based on the crystallographic data, all copper atoms in **A** are assigned to be in formal oxidation states of +1. To further corroborate this, XPS measurements of **A** were performed. The XPS measurements of **A** were then compared with those of the copper(I) acetate starting material and (Se-mCB)<sub>2</sub> as an analog of SeH-mCB due to the propensity of carborane chalcogenols to sublime under vacuum (Figure 4b). The Cu2 $p_{1/2}$  and Cu2 $p_{3/2}$  peaks of **A**, 952.7 eV and 932.8 eV respectively, are shifted to a lower binding energy relative to copper(I) acetate and are consistent with the more electron-rich<sup>69-70</sup> environment experienced by the copper(I) nuclei when interacting

with the *meta*-carborane selenolate. There are no satellite peaks present adjacent to the  $Cu2p_{1/2}$  peak, which are commonly found in XPS measurements of copper(II) containing materials,  $^{72}$  indicating that the copper(I) oxidation state is conserved during the course of the reaction. Peak-fitting of the Cu2p XPS signals further indicate the presence of a singular copper(I) environment, in agreement with the MicroED-derived structure (SI sec. 5e). Between (Se-mCB)<sub>2</sub> and **A**, there is no significant change in the Se3*d* peak binding energies, and peak-fitting again confirms only one selenium environment (SI sec. 5e). The XPS measurements further allude to the resistance of the copper(I) centers in **A** to oxidation by atmospheric oxygen despite the electron-rich environment imparted by the carborane selenolate,  $^{69.70}$  likely a result of the steric protection provided by the *meta*-carboranyl ligands as illustrated by the MicroED-derived single crystal structure.

In addition to XPS measurements, FTIR spectroscopy of **A** was used to confirm the absence of any residual starting materials. Specifically, the FTIR spectrum of **A** revealed a distinct loss of signal associated with the Se-H stretch present in the FTIR spectrum of SeH-mCB at 2400 cm<sup>-1</sup> (Figure 4c); though, the remaining cluster structure appears to be intact with only slight deviations in signals present in the fingerprint region (1250-600 cm<sup>-1</sup>). The presence of intact boron clusters in powder of A is further confirmed by diagnostic B-H resonances (2600 cm<sup>-1</sup>) in the spectrum. Furthermore, when comparing the FTIR spectrum of **A** with that of the copper(I) acetate starting material, there are no signals present in the formed material that could be correlated to the carbonoxygen double bond in copper(I) acetate, indicating that the acetate ligand is not present in the resulting hybrid material. Consistent with FTIR, TGA (Figure 4d) also revealed that there are no substantial solvent adducts in the **A** crystallites, as indicated by no significant mass loss until 300 °C, which is most likely associated with the decomposition of the *meta*-carborane selenolate and agrees with the single crystal MicroED structure.

To determine any effects the carborane dipole might impart on the structural behavior of the isolated microcrystals as well as the impact of chalcogenide (Se vs. S), we then studied the reaction of copper(I) acetate with 9-ortho-carborane selenol (9-SeH-oCB, B'), 9-meta-carborane thiol (9-SH-mCB, C'), and 9-ortho-carborane thiol (9-SH-oCB, D'). Notably, the molecular dipole in *ortho*-carborane is significantly larger in magnitude compared to that of *meta*-carborane.<sup>44,48,58</sup> Following similar procedures used in the synthesis of A, crystalline powders of Cu-[Se-oCB] (B), Cu-[S-mCB] (C), and Cu-[S-oCB] (D) were isolated as white/tan powders in 65%, 84%, and 69% isolated yields respectively (SI sec. 4) and characterized in a similar fashion to A. Despite the use of different carborane-based chalcogenols, FTIR, TGA, and XPS data of powders B, C, and D closely resemble the data obtained of A (SI sec. 6c-e, 7c-e, 8c-e), suggesting a molecular similarity. FTIR, for example, revealed that there is no starting carborane chalcogenol or copper(I) acetate present in the isolated powders **B-D**, with all materials exhibiting comparable thermal stabilities by TGA. While XPS indicates the copper(I) oxidation state is maintained during the formation of **B-D** with similar binding energy for the copper centers measured in **A** (Figure 5a). Additionally, solution-state <sup>1</sup>H and <sup>11</sup>B NMR spectroscopic measurement of materials **A-D** in dichloromethane further suggested similarities in the molecular structures of the materials and were consistent with FTIR and TGA measurements (SI sec. 10).

When comparing the PXRD data (SI sec. 6b, 7b, 8b) of all four materials, there are clear similarities in the molecular structures of **A-D** due to the closely matching diffractions from 5-25 20 regardless of chalcogen or carborane isomer (Figure 5b). When comparing the PXRD patterns of materials **A** and **B** (same chalcogen, different carborane isomer) there are some deviations, though they can be explained by the expected differences in molecular packing as a result of differing dipole-dipole interactions within the crystal (Figure 5c, SI sec. 11). In contrast, a closer

inspection of PXRD patterns (Figure 5c) for materials containing the same carborane isomer (*meta*:  $\mathbf{A}$ ,  $\mathbf{C}$ ; *ortho*:  $\mathbf{B}$ ,  $\mathbf{D}$ ) reveals nearly identical diffractions with negligible deviations between the data sets ( $< \pm 0.5 \ 2\theta$ ) that can be explained by the slight changes in d-spacing when the chalcogen is changed from selenium to sulfur (SI sec. 11). As expected, this data indicates that the carborane dipole plays a critical role in determining molecular packing of the material while the choice of chalcogen has a minor impact.

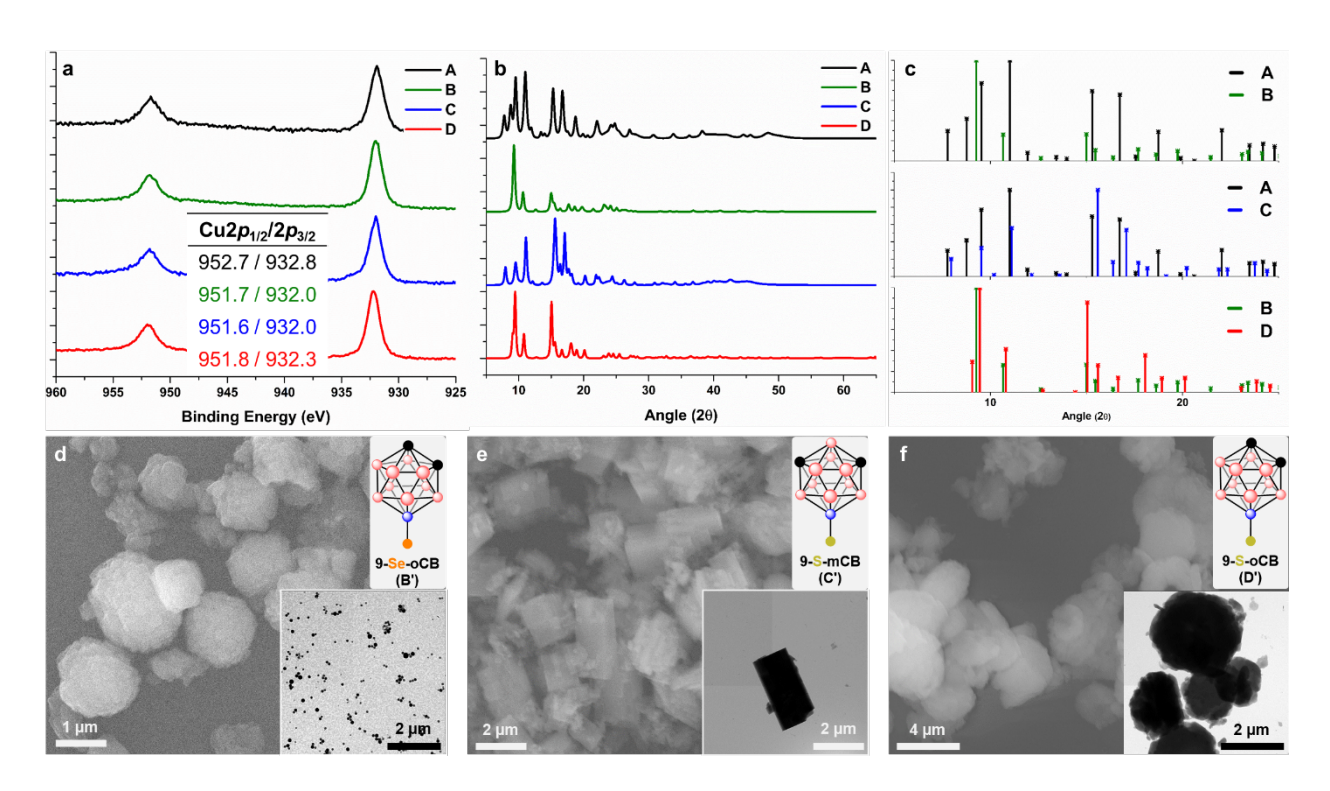


**Figure 5: a.** Comparison of  $Cu2p_{1/2}$  and  $Cu2p_{3/2}$  XPS measurements for materials **A-D. b.** Stacked PXRD patterns of materials **A-D. c.** Overlaid peak patterns for materials **A** and **B**, **A** and **C**, **B** and **D**. **d-f.** SEM and TEM (inset) images of **B-D**, respectively.

While FTIR, TGA, XPS, and PXRD suggested a molecular similarity between **A-D**, electron microscopy (SEM, TEM, Figure 5d-f, SI sec. 6-8a) revealed a distinct difference in crystallite morphology, largely as a function of carborane isomer while also affected by which chalcogen was present. **C** crystallites (Figure 5e) were similar in morphology to **A**, though would be more accurately described as square prisms, being generally thicker (2-3  $\mu$ m) and significantly

shorter (3-5 µm) in length. In contrast, materials **B** and **D**, which contain *ortho*-carborane-based chalcogenolates, favored the formation of spherical particles with two major phases present. In the case of **B**, while some larger particle aggregates (1.10  $\mu$ m  $\pm$  0.31) were present (Figure 5d), TEM revealed that a significant portion of the material consists of nanoscale particles (92 nm ± 25, Figure 5D inset); in contrast, **D** predominantly favored the formation of larger microscale particles  $(3.47 \, \mu \text{m} \pm 0.72, \text{Figure 5F})$ . MicroED measurements of **B** and **C** were attempted (SI sec. 6g, 7g), though the crystal morphologies were not easily amenable to electron diffraction. In the case of material **B**, the spherical nature of the particles, ultimately resulted in polycrystalline diffractions, while for material C the thickness of the crystallites inhibited electron diffraction, resulting in lowintensity diffractions.<sup>73</sup> The difference in morphologies (rods vs. spheres) between materials **A-D** can primarily be explained by inductive effect of the carborane cluster imparted onto the chalcogenolates, as well as the magnitude of the carborane dipole. In other words, the weaker dipole of the *meta*-carborane-containing ligands present in materials **A** and **C** unequivocally favors the formation of cubic, rod-like microcrystals. Whereas the stronger dipole of the ortho-carboranecontaining ligands present in materials **B** and **D** appears to limit long-range crystal growth and results in spherical microcrystals.

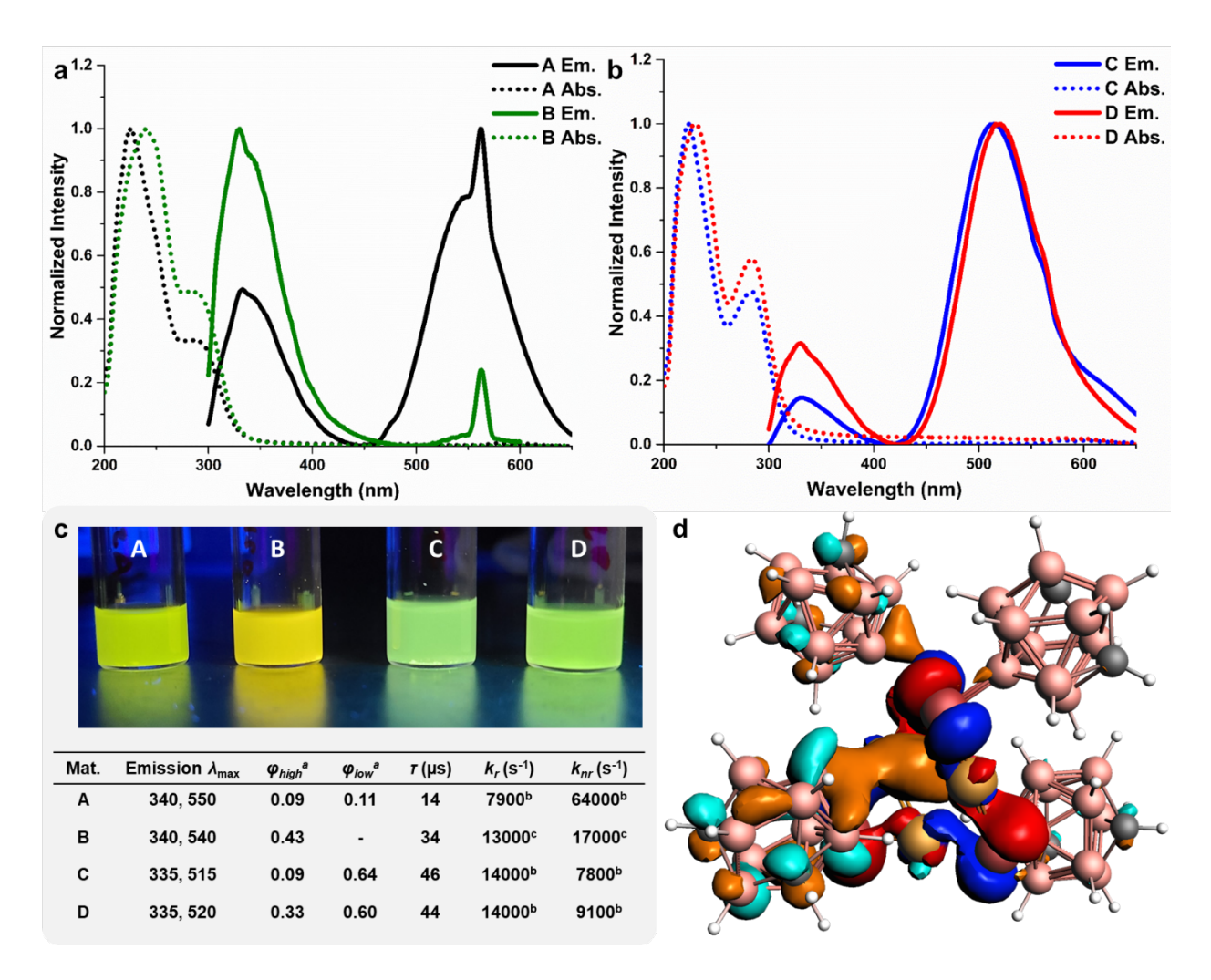


Figure 6: a-b. Emission (solid trace) and absorption (dotted trace) spectra of materials A-D. Due to the excitation wavelength used to obtain emission spectra (280 nm) for A-D, a peak is present at ~560 nm in all emission spectra that is not part of the emission of materials A-D. c. Images of emissive *iso*-propanol suspensions of A-D along with their respective emission wavelengths ( $\lambda_{max}$ ), quantum yields ( $\phi_{high}$ ,  $\phi_{low}$ ), lifetimes ( $\tau$ ), and calculated radiative ( $k_r$ ) and nonradiative ( $k_{nr}$ ) rate constants. d. HOMO (red, blue) and LUMO (orange, teal) of A, calculated on the crystallographically derived structure using B3LYP functional DZP basis set. The calculated HOMO-LUMO gap is 4.35 eV, corresponding to 285 nm.  $^a \phi_{high}$  and  $\phi_{low}$  are calculated based on the relative emission peak integrations for the high energy (low wavelength) and low energy (high wavelength) bands, respectively.  $^b$ Calculated using  $\phi_{low}$ .  $^c$ Calculated using  $\phi_{high}$ .

Materials consisting of metal-chalcogenolates, particularly those that are copper-based, often exhibit photoluminescence.<sup>74-77</sup> Similar properties are therefore expected for materials **A-D**. Differences in the electronic environment experienced by the copper-chalcogenide core are expected to arise as a function of both the carborane isomer (*meta-*, *ortho-*) and chalcogenide (Se,

S). Consequently, variations in the photophysical properties of each structure are expected. The normalized UV-Vis absorption spectra for uniform suspensions of A-D in iso-propanol all show two strong absorptions located at 220-240 nm and 280 nm (Figure 6a-b, dotted traces, SI sec. 5-8f). While the wavelengths of absorption do not vary greatly between compounds, differences in relative peak intensity are evident. Using the excitation wavelengths, as indicated by UV-Vis spectroscopy (220 nm and 280 nm), fluorescence measurements were subsequently obtained from the prepared iso-propanol suspensions. While the higher energy absorption (220 nm) was the most intense for all materials, no significant emission was associated with this excitation (SI sec. 5-8f). Notably, only the lower energy transition (280 nm) yielded any measurable emission (Figure 6ab, solid traces). For all four materials, emission was observed at 340 nm and at 450-650 nm, with the latter being significantly broader than the former and distinctly weaker in the case of **B**. Interestingly, when these materials are dissolved in polar aprotic organic solvents, all emissive properties are no longer present (SI sec. 12). To confirm the copper(I) selenide core in A was still intact upon dissolution, A was precipitated from solution by trituration with pentane and the emission of the as-synthesized crystals was fully regained (SI sec. 12), suggesting that luminescence is contingent upon restricted molecular motion that can be achieved in the solid state. This is further supported by the observation of luminescence in frozen solutions and in polymer matrices embedded with the materials. Notably, while the emission properties can be regained through these methods, they are red-shifted relative to the emission of the as-synthesized or triturated crystals (SI sec. 12). Such effects of temperature and aggregation/crystallization on emissive properties are commonly observed phenomena.<sup>78-80</sup>

To further understand the photophysical properties of these materials, quantum yield  $(\phi_{high}/\phi_{low})$  and lifetime ( $\tau$ ) measurements were performed on **A-D** as crystalline powders (see SI

for full details). The quantum yields associated with the high and low energy emissions ( $\phi_{high}/\phi_{low}$ ) were 0.09/0.11, 0.43/0.00, 0.09/0.64, and 0.33/0.60 for materials **A-D**, respectively (Figure 6c). Furthermore, the long lifetimes associated with the emissions (14, 34, 46, and 44  $\mu$ s for A-D, respectively), indicate that the luminescence is phosphorescent in nature, which is caused by the presence of the heavier copper, selenium, and sulfur atoms. Materials A and B exhibited overall weaker emission compared to C and D, favoring non-radiative relaxation from the excited state (Figure 6c). Furthermore, DFT calculations of A indicate that the emission most likely originates from a metal to ligand charge transfer (MLCT) between a copper(I) selenide-centered HOMO and a carborane selenolate-centered LUMO (Figure 6d, SI sec. 5h). While the differences in these photophysical properties are most closely correlated to the chalcogen present in the material (Se: A, B; S: C, D), there is a noticeable trend between materials within the same morphology category (rods, spheres) and thus contain the same carborane isomer. Notably, materials containing orthocarborane-based chalcogenolates (**B**, **D**), exhibited higher quantum yields compared to their metacarborane-containing counterparts (A, C). These results suggest that the tunable inductive effect<sup>7</sup> afforded by the carborane-based ligands using different isomers can be used to fine tune the electronic properties of copper(I) MOCHAs as demonstrated by the precise control over photophysical properties. This is consistent with what has been generally observed with other tunable carborane-based ligands in the context of organometallic Pt(II)-based luminescent emitters.60

# Conclusion

In summary, we demonstrate the synthesis and characterization of zero-dimensional carborane chalcogenolate-containing microcrystalline MOCHAs with tunable photoluminescent properties. We show that the nature of the carborane ligand dictates the crystallite morphology of

the resulting MOCHA, and is able to fine tune photophysical properties, such as quantum yield and emission lifetimes, without affecting the fundamental emission characteristics (Figure 6). Furthermore, MicroED has been used for the first time to structurally characterize this class of materials and has provided significant insight into the bonding arrangement between copper(I) and *meta*-carboranyl selenolate. In contrast to other MOCHA materials with an extended metal-chalcogenide core, MicroED has revealed that the synthesized carborane-structured MOCHAs consist of an unprecedented zero-dimensional Cu<sub>4</sub>Se<sub>4</sub> cluster that is representative of the smallest building block of bulk CuSe materials. This work therefore further establishes the utility of MicroED for hybrid material structure elucidation when reaching the limitations of more traditional structural determination methods.<sup>81-84</sup> This study furthermore highlights how the use of bulky, organomimetic, boron cluster ligands can lead to the formation of hybrid materials with unique structures and properties.<sup>35-57, 59-65, 85-100</sup>

# **Experimental Section**

#### **Materials**

*Ortho*-C<sub>2</sub>B<sub>10</sub>H<sub>12</sub> (Boron Specialties) was sublimed prior to use. *Meta*-C<sub>2</sub>B<sub>10</sub>H<sub>12</sub> (Katchem or Alfa Aesar) was used as is. Se<sub>2</sub>Cl<sub>2</sub> was synthesized according to previously reported procedures.<sup>101</sup> Anhydrous dichloromethane was obtained from a Grubbs column with activated alumina and copper catalyst. *Iso*-propanol (200 proof, Certified ACS Quality) was purchased from Fisher Sci. and dried over magnesium before use. Anhydrous copper(I) acetate (97%) was purchased from Strem Chemical Inc. and stored in a N<sub>2</sub>-filled glovebox at -30 °C. All other reagents were purchased from commercial vendors and used as is. Unless otherwise stated, all reactions were performed

under an inert atmosphere of N<sub>2</sub> either in a glovebox or using a Schlenk line, and all manipulations

were performed under ambient laboratory air, exposed to ambient light.

**Synthesis of Chalcogenols (A'-D')** 

All chalcogenols (A'-D') were prepared following literature procedures. 69,70 More detailed

synthetic procedures and representative <sup>1</sup>H and <sup>11</sup>B NMR spectra for each chalcogenol are provided

in SI sec. 3.

Synthesis and Isolation of Metal-Organic Chalcogenolate Assemblies (A-D)

In a N<sub>2</sub>-filled glovebox, chalcogenol (0.11 mmol 1.1 eq) and anhydrous copper(I) acetate (12 mg,

0.1 mmol, 1 eq) were added to an oven-dried 4 mL dram vial equipped with a stir bar and PTFE

septa cap. The vial was then sealed and transferred out of the glovebox before the addition of

anhydrous iso-propanol (1 mL) via syringe. The resulting suspension was immediately stirred at

~700 rpm and left to stir in the dark for 24 hours. After 24 hours, the as-synthesized materials were

isolated by sequential centrifugation (10 minutes at 2900xg), removal of supernatant, and

resuspension in iso-propanol (2 mL). This process was repeated a total of three times to ensure the

removal of any remaining chalcogenol. In the last cycle, instead of resuspension, the pellet was

dried on a high-vacuum Schlenk line to remove all volatiles. After drying, materials A-D were

afforded as analytically pure free-flowing powders of varying fluffiness in 69-84% isolated yields.

ASSOCIATED CONTENT

Crystallographic data are available from the Cambridge Crystallographic Data Centre, under the

reference number: CCDC 2121247 (A)

19

The following files are available free of charge.

Full synthetic procedures, additional materials characterization (PDF)

MicroED crystallographic data for **A** (CIF)

# **AUTHOR INFORMATION**

# **Corresponding Authors**

\*spokoyny@chem.ucla.edu

\*hosea@chem.ucla.edu

\*james.hohman@uconn.edu

# **ORCID**

Harrison A. Mills: 0000-0002-3621-9608

Christopher G. Jones: 0000-0003-4308-1368

Kierstyn P. Anderson: 0000-0002-0297-0727

Austin D. Ready: 0000-0001-8051-7568

Peter I. Djurovich: 0000-0001-6716-389X

Saeed I. Khan: 0000-0002-8641-9413

J. Nathan Hohman: 0000-0002-9777-6432

Hosea M. Nelson: 0000-0002-4666-2793

Alexander M. Spokoyny: 0000-0002-5683-6240

Notes

The authors declare no competing financial interests

# ACKNOWLEDGMENT

This work was supported by NSF Grants CHE-1846849 (NSF CAREER Award to A. M. S.) and

DGE-1650604. H. A. M. is a recipient of the UCLA Dissertation Year Fellowship and the M.

Frederick Hawthorne Inorganic Chemistry Dissertation Award. A. M. S. thanks Dreyfus Foundation for the Camille Dreyfus Teacher Scholar Award.

# REFERENCES

- (1) Rismaningsih, N.; Yamauchi, H.; Kameyama, T.; Yamamoto, T.; Morita, S.; Yukawa, H.; Uematsu, T.; Baba, Y.; Kuwabata, S.; Torimoto, T. Photoluminsecnce properties of quinary Ag-(In,Ga)-(S,Se) quantum dots with a gradiant allow structure for *in vivo* bioimaging. *J. Mater. Chem. C* **2021**, 9, 12791-12801.
- (2) Kanatzidis, M. G. Discovery-Synthesis, Design, and Predication of Chalcogenide Phases. *Inorg. Chem.* **2017**, *56*, 3158-3173.
- (3) Naskar, S.; Miethe, J. F.; Sánchez-Paradinas, S.; Schmidt, N.; Kanthasamy, K.; Behrens, P.; Pfnür, H.; Bigall, N. C. Photoluminescent Aerogels from Quantum Wells. *Chem. Mater.* **2016**, 28, 7, 2089-2099.
- (4) Liu, Y.; Weiss, N. O.; Duan, X.; Cheng, H.-C.; Huang, Y.; Duan, X. Van der Waals heterostructures and devices. *Nat. Rev. Mater.* **2016**, 1, 16042.
- (5) Matthews, P. D.; McNaughter, P. D.; Lewis, D. J.; O'Brien, P. Shining a light on transition metal chalcogenides for sustainable photovoltaics. *Chem. Sci.* **2017**, 8, 4177-4187.
- (6) Maruyama, M.; Nagashio, K.; Okada, S. Influence of Interlayer Stacking on Gate-Induced Carrier Accumulation in Bilayer MoS<sub>2</sub>. *ACS Appl. Electron. Mater.* **2020**, 2, 5, 1352-1357.

- (7) Giufredi, G.; Asset, T.; Liu ,Y.; Atanassov, P.; Fonzo, F. D. Transition Metal Chalcogenides as a Versatile and Tunable Platform for Catalytic CO<sub>2</sub> and N<sub>2</sub> Electroreduction. *ACS Mater. Au* **2021**, 1, 1, 6-36.
- (8) Eng, A. Y. S.; Ambrosi, A.; Sofer, Z.; Šimek, P.; Pumera, M. Electrochemistry of Transition Metal Dichalcogenides: Strong Dependence on the Metal-to-Chalcogen Composition and Exfoliation Method. *ACS Nano* **2014**, 8, 12, 12185-12198.
- (9) Zhang, D.; Cao, W.; Mao, B.; Liu, Y.; Li, F.; Dong, W.; Jiang, T.; Yong, Y.-C.; Shi, W. Efficient 0D/2D Heterostructured Photoctalysts with Zn-AgIn<sub>5</sub>S<sub>8</sub> Quantum Dots Embedded in the Ultrathin NiS Nanosheets for Hydrogen Production. *Ind. Eng. Chem. Res.* 2020, 59, 37.
- (10) Tulsky, E. G.; Long, J. R. Dimensional Reduction: A Practical Formalism for Manipulating Solid Structures. *Chem. Mater.* 2001, 13, 4, 1149-1166.
- (11) Coleman, J. N.; Lotya, M.; O'Neill, A.; Bergin, S. D.; King, P. J.; Khan, U.; Young, K.; Gaucher, A.; De, S.; Smith, R. J.; Shvets, I. V.; Arora, S. K.; Stanton, G.; Kim, H.-Y.; Lee, K.; Kim, G. T.; Duesberg, G. S.; Hallam, T.; Boland, J. J.; Wang, J. J.; Donegan, J. F.; Grunlan, J. C.; Moriarty, G.; Shmeliov, A.; Nicholls, R. J.; Perkins, J. M.; Grieveson, E. M.; Theuwissen, K.; McComb, D. W.; Nellist, P. D.; Nicolosi, V. Two-Dimensional Nanosheets Produced by the Liquid Exfoliation of Layered Materials. *Science* 2011, 331, 568-571.
- (12) Backes, C.; Szydłowska, B. M.; Harvey, A.; Yuan, S.; Vega-Mayora, V.; Davies, B. R.; Zhao, P.-L.; Hanlon, D.; Santos, E. J. G.; Katsnelson, M. I.; Blau, W. J.; Gadermaier,

- C.; Coleman, J. N. Production of Highly Monolayer Enriched Dispersion of Liquid-Exfoliated Nanosheets by Liquid Cascade Centrifugation. *ACS Nano* **2016**, 10, 1, 1589-1601.
- (13) Bodík, M.; Annušová, A.; Hagara, J.; Mičušík, M.; Omastová, M.; Kotlár, M.; Chlpík, J.; Cirák, J.; Švajdlenková, H.; Anguš, M.; Roldán, A. M.; Veis, P.; Jergal, M.; Majkova, E.; Šiffalovič, P. An elevated concentration of MoS<sub>2</sub> lowers the efficacy of liquid-phase exfoliation and triggers the production of MoO<sub>x</sub> nanoparticles. *Phys. Chem. Chem. Phys.* **2019**, 21, 12396-12405.
- (14) Manzeli, S.; Ovchinnikov, D.; Pasqeuir, D.; Yazyev, O. V.; Kis, A. 2D transition metal dichalcogenides. *Nat. Rev. Mater.* **2017**, 2, 17033.
- (15) Jia, C.; Lin, Z.; Huang, Y.; Duan, X. Nanowire Electronics: From Nanoscale to Macroscale. *Chem. Rev.* **2019**, 119, 15, 9074-9135.
- (16) Enright, M. J.; Dou, F. Y.; Wu, S.; Rabe, E. J.; Monahan, M.; Friedfeld, M. R.; Schlenker, C. W.; Cossairt, B. M. Seeded Growth of Nanoscale Semiconductor Tetrapods: Generality and the Role of Cation Exchange. *Chem. Mater.* **2020**, 32, 11, 4774-4784.
- (17) Li, T.; Liu, Y.-H.; Porter, S.; Goldberger, J. E. Dimensionally Reduced One-Dimensional Chains of TiSe<sub>2</sub>. *Chem. Mater.* **2013**, 25, 9, 1477-1479.
- (18) Chareev, D. A.; Evstingneeva, P.; Phuyal, D.; Man, G. J.; Rensmo, H.; Vasiliev, A.
   N.; Abdel-Hafiez, M. Growth of Transition Metal-Dichalcogenides by Solvent Evaporation Technique. *Cryst. Growth Des.* 2020, 20, 10, 6930-6938.

- (19) Ding, K.; Lu, H.; Zhang, Y.; Snedaker, M. L.; Liu, D.; Maciá-Agulló, J. A.; Stucky, G. D. Microwave Synthesis of Microstructured and Nanostructured Metal Chalcogenides from Elemental Precursors in Phosphonium Ionic Liquids. J. Am. Chem. Soc. 2014, 136, 44, 15465-15468.
- Yan, H.; Hohman, J. N.; Li, F. H.; Jia, C.; Solis-Ibarra, D.; Wu, B.; Dahl, J. E.
  P.; Carlson, R. M. K.; Tkachenko, B. A.; Fokin, A. A.; Schreiner, P. R.; Vailionis,
  A.; Kim, T. R.; Devereaux, T. P.; Shen, Z.-X.; Melosh, N. A. Hybrid Metal-Organic
  Chalcogenide Nanowires with Electrically Conductive Inorganic Core through
  Diamondoid-Directed Assembly. *Nat. Mater.* 2017, 16, 349-355.
- (21) Veselska, O.; Podbevšek, D.; Ledoux, G.; Fateeva, A.; Demessence, A. Intrinsic triple-emitting 2D copper thiolate coordination polymer as a ratiometric thermometer working over 400 K range. *Chem. Commun.* **2017**, 53, 12225.
- Yan, H.; Yang, F.; Pan, D.; Lin, Y.; Hohman, J. N.; Solis-Ibarra, D.; Li, F. H.; Dahl, J. E. P.; Carlson, R. M. K.; Tkachenko, B. A.; Fokin, A. A.; Schreiner, P. R.; Galli, G.; Mao, W. L.; Shen, Z.-X.; Melosh, N. A. Sterically controlled mechanochemistry under hydrostatic pressure. *Nature* 2018, 554, 505-510.
- (23) Veselska, O.; Demessence, A. d<sup>10</sup> coinage metal organic chalcogenolates: From oligomers to coordination polymers. *Coord. Chem. Rev.* **2018**, 355, 240-270.
- (24) Schriber, E. A.; Popple, D. C.; Yeung, M.; Brady, M. A.; Corlett, S. A.; Hohman,J. N. Mithrene Is a Self-Assembling Robustly Blue Luminescent Metal-Organic

- Chalcogenolate Assembly for 2D Optoelectronic Applications. *ACS Appl. Nano Mater.* **2018**, 1, 7, 3498-3508.
- (25) Eichhöfer, A.; Lebedkin, S. 1D and 3D Polymeric Manganese(II) Thiolato Complexes: Synthesis, Structure, and Properties of  $^3$ <sub>∞</sub>[Mn<sub>4</sub>(SPh)<sub>8</sub>] and  $^1$ <sub>∞</sub>[Mn(SMes)<sub>2</sub>]. *Inorg. Chem.* **2018**, 57, 602-608.
- Trang, B.; Yeung, M.; Popple, D. C.; Schriber, E. A.; Brady, M. A.; Kuykendall,
  T. R.; Hohman, J. N. Tarnishing Silver Metal into Mithrene. *J. Am. Chem. Soc.* 2018, 140,
  42, 13892-13903.
- (27) Popple, D. C.; Schriber, E. A.; Yeung, M.; Hohman, J. N. Competing Roles of Crystallization and Degradation of a Metal-Organic Chalcogenolate Assembly under Biphasic Solvothermal Conditions. *Langmuir* **2018**, 34, 47, 14265-14273.
- (28) Royappa, A. T.; Tran, C. M.; Papoular, R. J.; Khan, M.; Marbella, L. E.; Millstone, J. E.; Gembicky, M.; Chen, B.; Shepard, W.; Elkaim, E. Copper(I) and gold(I) thiolate precursors to bimetallic nanoparticles. *Polyhedron* **2018**, 155, 359-365.
- Xiao, Q.; Burg, A. J.; Zhou, Y.; Yan, H.; Wang, C.; Ding, Y.; Reed, E.; Miller, R.
  D.; Dauskardt, R. H. Electrically Conductive Copper Core-Shell Nanowires through
  Benzenethiol-Directed Assembly. *Nano Lett.* 2018, 18, 4900-4907.
- (30) Wang, J.; Li, Y.-L.; Wang, Z.-Y.; Zang, S.-Q. A robust wave-like silver-thiolate chain based metal-organic network: synthesis, structure and luminescence. *CrystEngComm* **2019**, 21, 2264.

- (31) Veselska, O.; Dessal, C.; Melizi, S.; Guillou, N.; Podbevšek, D.; Ledoux, G.; Elkaim, E.; Fateeva, A.; Demessence, A. New Lamellar Silver Thiolate Coordination Polymers with Tunable Photoluminescence Energies by Metal Substitution. *Inorg. Chem.* 2019, 58, 99-105.
- (32) Yeung, M.; Popple, D. C; Schriber, E. A.; Teat, S. J.; Beavers, C. M.; Demessence, A.; Kuykendall, T. R.; Hohman, J. N. Corrosion of Late- and Post-Transition Metals into Metal-Organic Chalcogenolates and Implications for Nanodevice Architectures. ACS Appl. Nano Mater. 2020, 3, 4, 3568-3577.
- (33) Vaidya, S.; Veselska, O.; Zhadan, A.; Diaz-Lopez, M.; Joly, Y.; Bordet, P.; Guillou, N.; Dujardin, C.; Ledoux, G.; Toche, F.; Chiriac, R.; Fateeva, A.; Horike, S.; Demessence, A. Transparent and luminescent glasses of gold thiolate coordination polymers. *Chem. Sci.* 2020, 11, 6815.
- (34) Paritmongkol, W.; Sakurada, T.; Lee, W. S.; Wan, R.; Müller, P.; Tisdale, W. A. Size and Quality Enhancement of 2D Semiconducting Metal-Organic Chalcogenolates by Amine Addition. *J. Am. Chem. Soc.* **2021**, 143, 48, 20256-20263
- (35) Yeager, L. J.; Saeki, F.; Shelly, K.; Hawthorne, M. F.; Garrell, R. L. A New Class of Self-Assembled Monolayers: *closo*-B<sub>12</sub>H<sub>11</sub>S<sup>3-</sup> on Gold. *J. Am. Chem. Soc.* **1998**, 120, 38, 9961-9962.
- (36) Baše, T.; Bastl, Z.; Plzák, Z.; Grygar, T.; Plešek, J.; Carr, M. J.; Malina, V.; Šubrt, J.; Boháček, J.; Večerníková, E.; Kříž, O. Carboranethiol-Modifed Gold Surfaces. A Study and Comparison of Modified Cluster and Flat Surfaces. *Langmuir* **2005**, 21, 17, 7776-7785.

- (37) Baše, T.; Bastl, Z.; Šlouf, M.; Klementová, M.; Šubrt, J.; Vetushka, A.; Ledinský, M.; Fejfar, A.; Macháček, J.; Carr, M. J.; Londesborough, M. G. S. Gold Micrometer Crystals Modifed with Carboranethiol Derivatives. J. Phys. Chem. C 2008, 112, 37, 14446-14455.
- (38) Hohman, J. N.; Zhang, P.; Morin, E. I.; Han, P.; Kim, M.; Kurland, A. R.; McClanahan, P. D.; Balema, V. P.; Weiss, P. S. Self-Assembly of Carboranethiol Isomer on Au{111}: Intermolecular Interactions Determined by Molecular Dipole Orientations. ACS Nano 2009, 3, 3, 527-536.
- (39) Baše, T.; Bastl, Z.; Havránek, V.; Lang, K.; Bould, J.; Londesborough, M. G. S.; Macháček, J.; Plešek, J. Carborane-thiol-silver interactions. A comparative study of the molecular protection of silver surfaces. *Surf. Coat. Tech.* **2010**, 204, 16-17, 2639-2646.
- (40) Hohman, J. N.; Claridge, S. A.; Kim; M.; Weiss, P. S. Cage molecules for self-assembly. *Mater. Sci. Eng. R Rep.* **2010**, 70, 3-6, 188-208.
- (41) Lübben, J. F.; Baše, T.; Rupper, P.; Künniger, T.; Macháček, J.; Guimond, S. J. Colloid Interface Sci. 2011, 354, 1, 168-174.
- (42) Bould, J.; Macháček, J.; Londesborough, M. G. S.; Macías, R.; Kennedy, J. D.; Bastl, Z.; Rupper, P.; Baše, T. Decaborane Thiols as Building Blocks for Self-Assembled Monolayers on Metal Surfaces. *Inorg. Chem.* **2012**, 51, 3, 1685-1694.
- (43) Baše, T.; Bastl, Z.; Havránek, V.; Macháček, J.; Langecker, J.; Malina, V. Carboranedithiols: Building Blocks for Self-Assembled Monolayers on Copper Surfaces.

  \*Langmuir 2012\*, 28, 34, 12518-12526.

- (44) Kim, J.; Rim, Y. S.; Liu, Y.; Serino, A. C.; Thomas, J. C.; Chen, H.; Yang, Y.; Weiss, P. S. Interface Control in Organic Electronics Using Mixed Monolayers of Carboranethiol Isomers. *Nano Lett.* 2014, 14, 2946-2951.
- (45) Vetushka, A.; Bernard, L.; Guseva, O.; Bastl, Z.; Plocek, J.; Tomandl, I.; Fejfar, A.; Baše, T.; Schmutz, P. Adsorption of oriented carborane dipole on a silver surface. *Phys. Solid State B* **2015**, 253, 3, 591-600.
- (46) Thomas, J. C.; Boldog, I.; Auluck, H. S.; Bereciartua, P. J.; Dušek, M.; Macháček, J.; Bastl, Z.; Weiss, P. S.; Baše, T. Self-Assembled p-Carborane Analogue of p-Mercaptobenzoic Acid on Au{111}. Chem. Mater. 2015, 27, 15, 5425-5435.
- (47) Schwartz, J. J.; Mendoza, A. M.; Wattanatorn, N.; Zhao, Y.; Nguyen, V. T.; Spokoyny, A. M.; Mirkin, C. A.; Baše, T.; Weiss, P. S. Surface Dipole Control of Liquid Crystal Alignment. *J. Am. Chem. Soc.* **2016**, 138, 18, 5957-5967.
- (48) Serino, A. C.; Anderson, M. E.; Saleh, L. M. A.; Dziedzic, R. M.; Mills, H.; Heindenreich, L. K.; Spokoyny, A. M.; Weiss, P. S. Work Function Control of Germanium through Carborane-Carboxylic Acid Surface Passivation. *ACS Appl. Mater. Interfaces* **2017**, 9, 34592-34596.
- Thomas, J. C.; Goronzy, D. P.; Serino, A. C.; Auluck, H. S.; Irving, O. R.; Jimenez-Izal, E.; Deirmenjian, J. M.; Macháček, J.; Sautet, P.; Alexandrova, A. N.; Baše, T.; Weiss, P. S. Acid-Base Control of Valency within Carboranedithiol Self-Assembled Monolayer:
  Molecules Do the Can-Can. ACS Nano 2018, 12, 3, 2211-2221.

- (50) Wang, S.; Goronzy, D. P.; Young, T. D.; Wattanatorn, N.; Stewart, L.; Baše, T.; Weiss, P. S. Formation of Highly Ordered Terminal Alkyne Self-Assembled Monolayers on the Au{111} Surface through Substitution of 1-Decaboranethiolate. *J. Phys. Chem. C* 2019, 123, 2, 1348-1353.
- (51) Hladík, M.; Vetushka, A.; Fejfar, A.; Vázquez, H. Tuning of the gold work function by carborane films studied using density functional theory. *Phys. Chem. Chem. Phys.* **2019**, 21, 6178-6185.
- (52) Goronzy, D. P.; Staněk, J.; Avery, E.; Guo, H.; Bastl, Z.; Dušek, M.; Gallup, N. M.; Gün, S.; Kučeráková, M.; Levandowski, B. J.; Macháček, J.; Šícha, V.; Thomas, J. C.; Yavuz, A.; Houk, K. N.; Danişman; Mete, E.; Alexandrova, A. N.; Baše, T.; Weiss, P. S. Influence of Terminal Carboxyl Groups on the Structure and Reactivity of Functionalized *m*-Carboranethiolate Self-Assembled Monolayers. *Chem. Mater.* 2020, 32, 15, 6800-6809.
- (53) Li, Y.-L.; Wang, Z.-Y.; Ma, X.-H.; Luo, P.; Du, C.-X.; Zang, S.-Q. Distinct photophysical properties in atom-precise silver and copper nanocluster analogues. *Nanoscale* **2019**, 11, 5151-5157.
- (54) Saini, A.; Saha, A.; Viñas, C.; Teixidor, F. The key to controlling the morphologies of quantum nanocrystals: spherical carborane ligands. *Chem. Commun.* **2019**, 55, 9817-9820.
- (55) Wang, Q.-Y.; Wang, J.; Wang, S.; Wang, Z.-Y.; Cao, M.; He, C.-L.; Yang, J.-Q.; Zang, S.-Q.; Mak, T. C. W. *o*-Carborane-Based and Atomically Precise Metal Clusters as Hypergolic Materials. *J. Am. Chem. Soc.* **2020**, 142, 28, 12010-12014.

- Valušová, E.; Kaňuchová, M.; Baše, T.; Víglaský, V.; Antalík, M. The Au<sub>25</sub>(SR)<sub>18</sub> cluster carrying icosahedral dodecaborate and glutathione ligands: A spectroscopic view. *J. Phys. Chem. Solids* **2021**, 150, 109838.
- (57) Jana, A.; Jash, M.; Poonia, A. K.; Paramasivam, G.; Islam, M. R.; Chakraborty, P.; Antharjanam, S.; Machacek, J.; Ghosh, S.; Adarsh, K. N. V. D.; Base, T.; Pradeep, T. Light-Activated Intercluster Conversion of an Atomically Precise Silver Nanocluster. ACS Nano 2021, 15, 10, 15781-15793.
- (58) For a general overview of carboranes, see: Grimes, R. N. *Carboranes*, 3<sup>rd</sup> ed; Elsevier: Oxford, 2016.
- (59) Eleazer, B. J.; Peryshkov, D. V. Coordination Chemistry of Carborane Cluster: Metal-Boron Bonds in Carborane, Carobranyl, and Carboryne Complexes. *Comments Inorg. Chem.* 2018, 38, 3, 79-109.
- (60) Kirlikovali, K. O.; Axtell, J. C.; Anderson, K. P.; Djurovich, P. I.; Rheingold, A. L.; Spokoyny, A. M. Fine-Tuning Electronic Properties of Luminescent Pt(II) Complexes via Vertex-Differentiated Coordination of Sterically Invariant Carborane-Based Ligands.
  Organometallics 2018, 37, 18, 3122-3131.
- (61) Eleazer, B. J.; Smith, M. D.; Popov, A. A.; Peryshkov, D. V. Expansion of (BB)>Ru metallacycle with coinage metal cations: formation of B-M-Ru-B (M = Cu, Ag, Au) dimetalacyclodiboryls. *Chem. Sci.* **2018**, 9, 2601-2608.

- (62) Zhang, J.; Cao, B.; Ding, Y.; Chang, J.; Li, S.; Chen, X. Syntheses and Structure of Group 10 Metal POCOP Pincer Complexes bearing A Mercapto-o-carborane Auxiliary Ligand. *ChemistrySelect* **2019**, 4, 4, 1292-1297.
- (63) Eleazer, B. J.; Smith, M. D.; Peryshkov, D. V. Reaction of a ruthenium B-carboranyl hydride complex and BH<sub>3</sub>(SMe<sub>2</sub>): Selective formation of a pincer-supported metallaborane LRu(B<sub>3</sub>H<sub>8</sub>). *Tetrahedron* **2019**, 75, 11, 1471-1474.
- (64) Zhang, K.; Shen, Y.; Yang, X.; Liu, J.; Jiamg, T.; Finney, N.; Spingler, B.; Duttwyler, S. Atomically Defined Monocarborane Copper(I) Acetylides with Structural and Luminescence Properties Tuned By Ligand Sterics. *Chem. Eur. J.* 2019, 25, 37, 8754-8759.
- (65) Mandal, D.; Rosair, G. M. Exploration of Bis(nickelation) of 1,1'-Bis(o-carborane).

  Crystals 2021, 11, 1, 16.
- (66) Dziedzic, R. M.; Spokoyny A. M. Metal-Catalyzed Cross-Coupling Chemistry with Polyhedral Boranes. *Chem. Commun.* **2019**, 55, 430-442.
- (67) Quan, Y.; Tang, C.; Xie, Z. Nucleophilic substitution: a facile strategy for selective B-H functionalization of carboranes. *Dalton Trans.* **2019**, 48, 7494-7498.
- (68) Quan, Y.; Xie, Z. Controlled functionalization of *o*-carborane *via* transition metal catalyzed B-H activation. *Chem. Soc, Rev.* **2019**, 48, 3660-3673.

- (69) Spokoyny A. M.; Machan, C. W.; Clingerman, D. J.; Rosen, M. S.; Wiester, M. J.; Kennedy, R. D.; Stern, C. L.; Sarjeant, A. A.; Mirkin, C. A. A coordination chemistry dichotomy for icosahedral carborane-based ligands. *Nat. Chem*, **2011**, 3, 590-596.
- Mills, H. A.; Alsarhan, F.; Ong, T.-C.; Gembicky, M.; Rheingold, A. L.; Spokoyny,
   A. M. Icosahedral m-Carboranes Containing Exopolyhedral B-Se and B-Te Bonds. *Inorg. Chem.* 2021, 60, 24, 19165-19174.
- (71) The simulated PXRD pattern of **A** was simulated using Mercury 4.3.0 with the MicroED-derived structure and .cif file.
- (72) Biesinger, M. C. Advanced analysis of copper X-ray photoelectron spectra. *Surf. Interface Anal.* **2017**, 49, 13, 1325-1334.
- (73) Zou, X.; Hovmóller, S.; Oleynikov, P. *Electron Crystallography: Electron Microscopy and Electron Diffraction*, Oxford Scholarship Online, 2012.
- (74) Crespo, O.; Gimeno, M. C.; Lagun, A.; Larraz, C.; Villacampa, M. D. Highly Luminescent Gold(I)-Silver(I) and Gold(I)-Copper(I) Chalcogenide Clusters. *Chem. Eur. J.* **2006** 13, 1, 235-246.
- (75) Kriegel, I.; Jiang, C.; Rodríguez-Fernández, J.; Schaller, R. D.; Talapin, D. V.;
  Como, E. D.; Feldmann, J. Tuning the Excitonic and Plasmonic Properties of Copper
  Chalcogenide Nanocrystals. J. Am. Chem. Soc. 2012, 134, 3, 1583-1590.

- (76) Singh, A.; Singh, S.; Levcenko, S.; Unold, T.; Laffir, F.; Ryan, K. M. Compositionally Tunable Photoluminescence Emission in Cu<sub>2</sub>ZnSn(S<sub>1-x</sub>Se<sub>x</sub>)<sub>4</sub> Nanocrystals.

  Angew. Chem. Int. Ed. **2013**, 52, 35, 9120-9124.
- (77) Polgar, A. M.; Zhang, A.; Mack, F.; Weigend, F.; Lebedkin, S.; Stillman, M. J.; Dorrigan, J. F. Tuning the Metal/Chalcogen Composition in Copper(I)-Chalcogenide Clusters with Cyclic (Alkyl)(amino)carbene Ligands. *Inorg. Chem.* **2019**, 58, 5, 338-3348.
- (78) Mei, J.; Leung, N. L. C.; Kwok, R. T. K.; Lam, J. W. Y.; Tang, B. Z. Aggregation-Induced Emission: Together We Shine, United We Soar! *Chem. Rev.* **2015**, 115, 21, 11718-11940.
- (79) Chin, P. T. K.; Donegá, C. d. M.; van Bavel, S. S.; Meskers, S. C. J.; Sommerdijk, N. A. J. M.; Janssen, R. A. Highly Luminescent CdTe/CdSe Collodial Heteronanocrystals with Temperature-Dependent Emission Color. *J. Am. Chem. Soc.* 2007, 129, 48, 14880-14886.
- (80) Lu, W.; Tarekegne, A. T.; Ou, Y.; Kamiyama, S.; Ou, H. Temperature-dependent photoluminescence properties of porous fluorescent SiC. *Scientific Reports* **2019**, 9, 16333.
- (81) Jones, C. G.; Asay, M.; Kim, L. J.; Kleinsasser, J. F.; Saha, A.; Fulton, T. J.; Berkeley, K. R.; Cascio, D.; Malyutin, A. G.; Conley, M. P.; Stoltz, B. M.; Lavallo, V.; Rodríguez, J. A.; Nelson, H. M. Characterization of Reactive Organometallic Species via MicroED. ACS Cent. Sci. 2019, 5, 9, 1507-1513.
- (82) Samkian, A. E.; Kiel, G. R.; Jones, C. G.; Bergman, H. M.; Oktaweic, J.; Nelson, H. M.; Tilley, T. D. Elucidation of Diverse Solid-State Packing in a Family of Electron-Deficient Expanded Helicenes via Microcrystal Electron Diffraction (MicroED). *Angew. Chem. Int. Ed.* 2021, 60, 5, 2493-2499.

- (83) Meng, Z.; Jones, C. G.; Farid, S.; Khan, I. U.; Nelson, H. M.; Mirica, K. A. Unraveling the Electrical and Magnetic Properties of Layered Conductive Metal-Organic Framework with Atomic Precision. *Angew. Chem. Int. Ed.* **2022**, 61, 6 e202113569.
- (84) Doyle, L. R.; Thompson, E. A.; Burnage, A. L.; Whitwood, A. C.; Jenkins, H. T.; Macgregor, S. A.; Weller, A. S. MicroED characterization of a robust cationic σ-alkane complex stabilized by the [B(3,5-(SF<sub>5</sub>)<sub>2</sub>C<sub>6</sub>H<sub>3</sub>)<sub>4</sub>] anion, via on-grid solid/gas single-crystal to single-crystal reactivity. *Dalton Trans*. **2022**, 51, 3661-3665.
- (85) Keener, M.; Hunt, C.; Carroll, T. G.; Kampel, V.; Dobrozetsky, R.; Hayton, T. W.; Ménard, G. Redox-switchable carboranes for uranium capture and release. *Nature* 2020, 577, 652-655.
- (86) Kim, T.; Kim, H.; Lee, K. M.; Lee, Y. S.; Lee, M. H. Phosphorescence Color Tuning of Cyclometallated Iridium Complexes by *o*-Carborane Substitution. *Inorg. Chem.* **2013**, 52, 1, 160-168.
- (87) Böhling, L.; Brockhinke, A.; Kahlert, J.; Weber, L.; Harder, R. A.; Yufit, D. S.; Howard, J. A. K.; MacBride, J. A. H.; Fox, M. A. Substituent Effects on the Fluorescence Properties of *ortho*-Carboranes: Unusual Emission Behaviour in *C*-(2'-Pyridyl)-*ortho*-carboranes. *Eur. J. Inorg. Chem.* **2016**, 3, 403-412.
- (88) Axtell, J. A.; Kirlikovali, K. O.; Djurovich, P. I.; Jung, D.; Nguyen, V. T.; Munekiyo, B.; Royappa, A. T.; Rheingold, A. L.; Spokoyny, A. M. Blue Phosphorescent Zwitterionic Iridium(III) Complexes Featuring Weakly Coordinating *nido*-Carborane-Base Ligands. *J. Am. Chem. Soc.* **2016**, 138, 48, 15758-15765.

- (89) Shi, C.; Sun, H.; Jiang, Q.; Zhao, Q.; Wang, J.; Huang, W.; Yan, H. Carborane tuning of photophysical properties of phosphorescent iridium(III) complexes. *Chem. Commun.* **2013**, 49, 4746-4748.
- (90) Tsang, M. Y.; Viñas, C.; Teixidor, F.; Planas, J. G.; Conde, N.; SanMartin, R.; Herrero, M. T.; Domínguez, E.; Lledós, A.; Vidossich, P.; Choquesillo-Lazarte, D. Synthesis, Structure, and Catalytic Application of *ortho-* and *meta-*Carboranyl Based NBN Pincer-Pd Complexes. *Inorg. Chem.* 2014, 53, 17, 9284-9295.
- (91) Jung, D.; Saleh, L. M. A.; Berkson, Z. J.; El-Kady, M. F.; Hwang, J. Y.; Mohamed, N.; Wixtrom, A. I.; Titarenko, E.; Shao, Y.; McCarthy, K.; Guo, J.; Martini, I. B.; Kraemer, S.; Wegner, E. C.; Saint-Cricq, P.; Ruehle, B.; Langeslay, R. R.; Delferro, M.; Brosmer, J. L.; Hendon, C. H.; Gallagher-Jones, M.; Rodriguez, J.; Chapman, K. W.; Miller, J. T.; Duan, X.; Kaner, R. B.; Zink, J. I.; Chmelka, B. F.; Spokoyny, A. M. A molecular cross-linking approach for hybrid metal oxides. *Nat. Mat.* 2018, 17, 341-348.
- (92) Farha, O. K.; Spokoyny, A. M.; Mulfort, K. L.; Hawthorne, M. F.; Mirkin, C. A.; Hupp, J. T. Synthesis and Hydrogen Sorption Properties of Carborane Based Metal-Organic Framework Materials. J. Am. Chem. Soc. 2007, 129, 42, 12680-12681.
- (93) Zhang, Y.; Hu, J.; Krishna, R.; Wang, L.; Yang, L.; Cui, X.; Duttwyler, S.; Xing, H. Rational Design of Microporous MOFs with Anionic Boron Cluster Functionality and Cooperative Dihydrogen Binding Sites for Highly Selective Capture of Acetylene. *Angew. Chem. Int. Ed.* 2020, 59, 40, 17664-17669.
- (94) Mukherjee, S.; Thilagar, P. Boron cluster in luminescent materials. *Chem. Commun.* **2016**, 52, 1070-1093.

- (95) Núñez, R.; Tarrés, M.; Ferrer-Ugalde, A.; Fabrizi de Biani, F.; Teixidor, F. Electrochemistry and Photoluminescence of Icosahedral Carboranes, Boranes, Metallacarboranes, and Their Derivatives. *Chem. Rev.* **2016**, 116, 23, 14307-14378.
- (96) Spokoyny, A. M. New ligand platforms featuring boron-rich clusters as organomimetic substituents. *Pure Appl. Chem.* **2013**, 85, 5, 903-919.
- (97) Dash, B. P.; Satapathy, R.; Maguire, J. A.; Hosmane, N. S. Polyhedral boron clusters in materials science. *New J. Chem.* **2011**, 35, 1955-1972.
- (98) Gan, L.; Chidambaram, A.; Fonquernie, P. G.; Light, M. E.; Choquesillo-Lazarte, D.; Huang, H.; Solano, E.; Fraile, J.; Viñas, C.; Teixidor, F.; Navarro, J. A. R.; Stylianou, K. C.; Planas, J. G. A Highly Water-Stable meta-Carborane-Based Copper Metal-Organic Framework for Efficient High-Temperature Butanol Separation. *J. Am. Chem. Soc.* 2020, 142, 18, 8299-8311.
- (99) Choi, S.; Lee, H.-E.; Ryu, C. H.; Lee, J.; Yoon, M.; Kim, Y.; Park, M. H.; Lee, K. M.; Kim, M. Synthesis of o-carborane-functionalized metal-organic frameworks through ligand exchanges for aggregation-induced emission in the solid state. *Chem. Commun.* 2019, 55, 11844-11847.
- (100) Fisher, S. P.; Tomich, A. W.; Lovera, S. O.; Kleinsasser, J. F.; Guo, J.; Asay, M. J.; Nelson, H. M.; Lavallo, V. Nonclassical Applications of closo-Carborane Anions: From Main Group Chemistry and Catalysis to Energy Storage. *Chem. Rev.* 2019, 119, 14, 8262-8290.
- (101) Lenher, V.; Kao, C. H. The Preparation of Selenium Monochloride and Monobromide. *J. Am. Chem. Soc.* **1925**, 47, 3, 772-774.

# **Graphical Abstract (TOC)**

